A Mixed Lubrication Analysis of a Thrust bearing with Fractal Rough Surfaces

Xiaohan Zhang[1], Yang Xu[2], Robert L. Jackson[3]

1. School of Mechanical & Automotive Engineering, Qingdao University of Technology, Qingdao, 266520, China

2. Department of Systems, Power and Energy, University of Glasgow, Glasgow, G12 8QQ, UK

3. Department of Mechanical Engineering, Auburn University, Auburn, AL 36849, USA

xzz0030@tigermail.auburn.edu

Abstract: Fractal descriptions of rough surfaces are widely used in tribology. The fractal dimension, *D*, is an important parameter which has been regarded as instrument and scale independent, although recent findings bring this into question. A thrust bearing is analyzed in the mixed lubrication regime while considering the fractal nature. Surface data obtained from a thrust bearing surface is characterized and used to calculate the fractal dimension value by the roughness-length method. Then these parameters are used to generate different rough surfaces via a filtering algorithm. By comparing the predicted performance between the measured surface and generated fractal surfaces, it is found that the fractal dimension must be used carefully when characterizing the tribological performance of rough surfaces, and other parameters need to be found.

Key words: fractal analysis; fractal dimension; surface generation; rough surfaces

Introduction

The thrust bearing is widely used in many rotary industrial applications. A thrust bearing is used to carry the axial or thrust load placed on a shaft. The roughness of its surface can affect the wear, friction and sealing behavior of contact surfaces. Typically, the study of thrust bearings mainly focused on the groove effects [1], its behavior under mixed lubrication or hydrodynamic lubrication conditions [1, 2], and the thermal effects [3, 4, 5]. Only a few studies have combined

Nomenclature

A	Amplitude parameter
D	Fractal dimension
dr, $d\theta$	Radius and the angle between two nodes
E'	Equivalent Young's modulus
f_c	Cut-off frequency
H	Hurst exponent
H^*	The ratio of the nominal film thickness to the surface roughness
h	Surface separation between the surface and the mean asperity level
h_0	Initial surface separation
ifft2	Discrete inverse Fourier transform function in Matlab
K	Kurtosis
L	Length of measured surface
L_{total}	Total load carrying capacity
L_f	Load carrying capacity from fluid part
L_s	Load carrying capacity from solid contact part
N	Relative sliding velocity
n_w	Total number of square windows
P	Unit load
p	Total pressure
p_f	Pressure from fluid part
p_s	Pressure from solid contact part
p_k^i	Pressure of the k_{th} point in the i_{th} iteration
q_0	Cut-off wave vector
q_x, q_y	Frequencies in x and y direction
R	Asperity radius
r_o	Outer radius of the thrust bearing
Sk	Skewness
T_{total}	Total torque
T_f	Torque from fluid part
T_s	Torque from solid contact part
u	Deflection of the surface
w	Side length
z	Height of the measured point
z_j	Residuals of the asperity height
$\bar{z}$	Mean residual asperity height
λ	Wavelength
λ_u	Effective upper wavelength
ϕ_r	Pressure flow factors in r direction
ϕ_θ	Pressure flow factors in θ direction

ϕ_s Shear flow factor

μ Expectation of surface distribution

η Viscosity of lubrication

η_s Asperity density

σ Standard deviation of the surface height

σ_s Standard deviation of the asperity heights

ω Angular velocity

the mixed lubrication analysis and the surface roughness effects together to analyze the behavior of a thrust bearing [6].

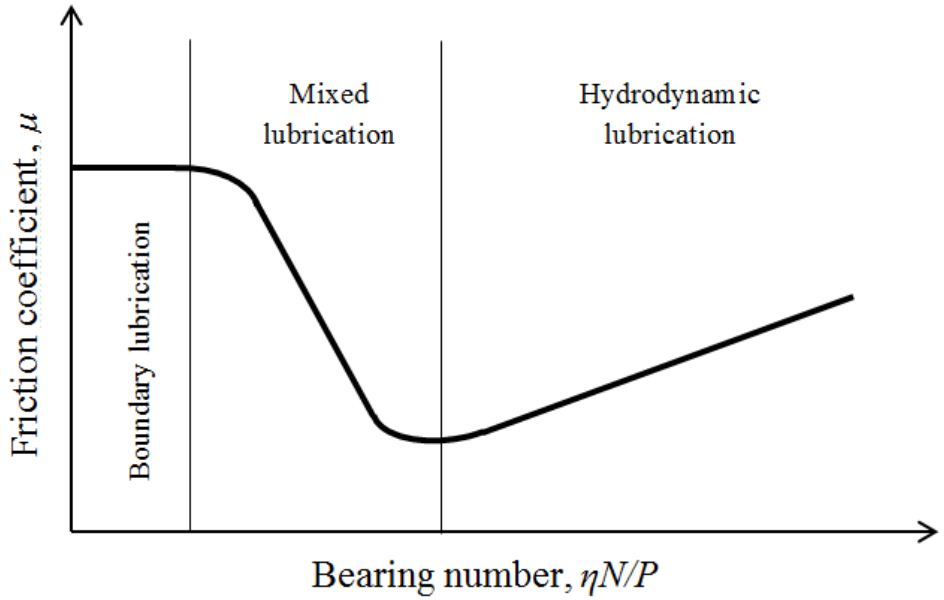

Fig.1- Schematic of a Stribeck curve

Fig.1 shows the Stribeck curve. It is basically a curve describing the relationship between the coefficient of friction and the bearing number (defined as the relative sliding velocity, N, times the viscosity of the lubricant, η, per unit load, P). According to the Stribeck curve, lubricated surface contact can be categorized by three regimes: the boundary lubrication regime, the mixed lubrication regime and the hydrodynamic lubrication regime. Even with the existence of a lubricating film between two contact surfaces, some surface asperities in the thrust bearing can

still come into contact because of the surface roughness. Therefore, the contact between the thrust bearing surfaces is often considered to be in the mixed lubrication regime.

The fractal descriptions of rough surfaces are widely used [7-10] since Mandelbrot first proposed the idea of fractal geometry [11]. The fractal dimension, *D*, which is a parameter from the fractal geometry, has become an important tool in characterizing the surface roughness. The fractal dimension describes the space occupation of a geometry (i.e. for a perfect line, the fractal dimension is one ($D = 1$), for a surface, it is two ($D = 2$) and for a space, it is three ($D = 3$)). Fractal geometry can be used to describe non-Euclidean geometries in between 1, 2 and 3 with non-integer fractal dimension values, *D*.

The aim of this work is to combine the elasto-hydrodynamic lubrication and rough surface contact effects together to analyze the effectiveness of the fractal methods in characterizing the thrust bearing surface, although the results may also be applicable to other tribological interfaces.

Theory

Normally, the mixed lubrication contact can be divided into hydrodynamic lubrication and solid contact. In our work, the flow-factor modified Reynolds equation [12, 13] is used to model the hydrodynamic lubrication part of the contact and the Greenwood & Williamson (GW) model [14] is used to calculate the pressure from solid contact.

According to Patir and Cheng [12, 13], the fluid pressure, p_f, generated by the hydrodynamic part can be calculated by the modified Reynolds equation in the cylindrical coordinates [15]:

$$\frac{\partial}{\partial r}\left(\phi_r \frac{rh^3}{\eta}\frac{\partial p_f}{\partial r}\right) + \frac{1}{r}\frac{\partial}{\partial \theta}\left(\phi_\theta \frac{h^3}{\eta}\frac{\partial p_f}{\partial \theta}\right) = 12\left(\frac{r\omega}{2}\frac{\partial h}{\partial \theta} - \frac{r\omega}{2}\sigma\frac{\partial \phi_s}{\partial \theta}\right) \quad (1)$$

$$\phi_\theta = \phi_r = 1 - 0.9\exp\left(-0.56H^*\right) \quad (2)$$

$$\phi_s = \begin{cases} 1.899{H^*}^{0.98} exp\left(-0.92H^* + 0.05{H^*}^2\right) & H \le 5 \\ 1.126\exp(-0.25H^*) & H > 5 \end{cases} \quad (3)$$

where ϕ_r and ϕ_θ are the pressure flow factors and ϕ_s is the shear flow factor (they are all calculated according to [16]); $H^* = h/\sigma$ is the ratio of the surface separation between the surface and the mean asperity level h to the standard deviation of the surface height σ; η is the viscosity of the lubricants. The flow factors consider how the roughness obstructs the flow between surfaces in close proximity. The work assumes that the surfaces are isotropic. Therefore, the equations of flow factors for isotropic surfaces are used based on Patir and Cheng [12, 13]. The Reynolds equation is solved by the finite difference method in our work (identical to the method used in [6]).

The expression of the solid contact pressure, p_s, calculated by the Greenwood & Williamson (GW) model [14] is:

$$p_s = \frac{4}{3}\eta_s E'\sqrt{R}\int_h^\infty (z-h)^{\frac{3}{2}}\varphi(z)dz \quad (4)$$

$$\varphi(z) = \frac{1}{\sqrt{2\pi}\sigma_s} exp\left(-\frac{z^2}{2\sigma_s^2}\right) \quad (5)$$

where $\varphi(z)$ is called the probability function; η_s is the asperity density; E' is the equivalent Young's modulus; σ_s is the standard deviation of the asperity heights, $\sigma_s = \left(1 - \frac{0.8968}{\alpha}\right)^{0.5}\sigma$ and α is called the bandwidth parameter introduced by Nayak [17]; R is the same radius of all asperity summits had, which means the asperity summits have the same radius of curvature. Eq. (4) is solved by the Simpson quadrature in our work.

The negative pressure is set to be zero during the calculation of the pressure, which means the Reynolds Boundary condition for cavitation is used. After the pressure and shear stress are obtained from the calculation above, the torque and load carrying capacity of the measured surface from the thrust bearing and the generated surfaces can be calculated and compared. Fig.2 shows

the flow chart of the numerical process for the mixed lubrication analysis. The fluid lubrication and solid contact are solved simultaneously as a coupled problem using this iterative process according to Fig.2.

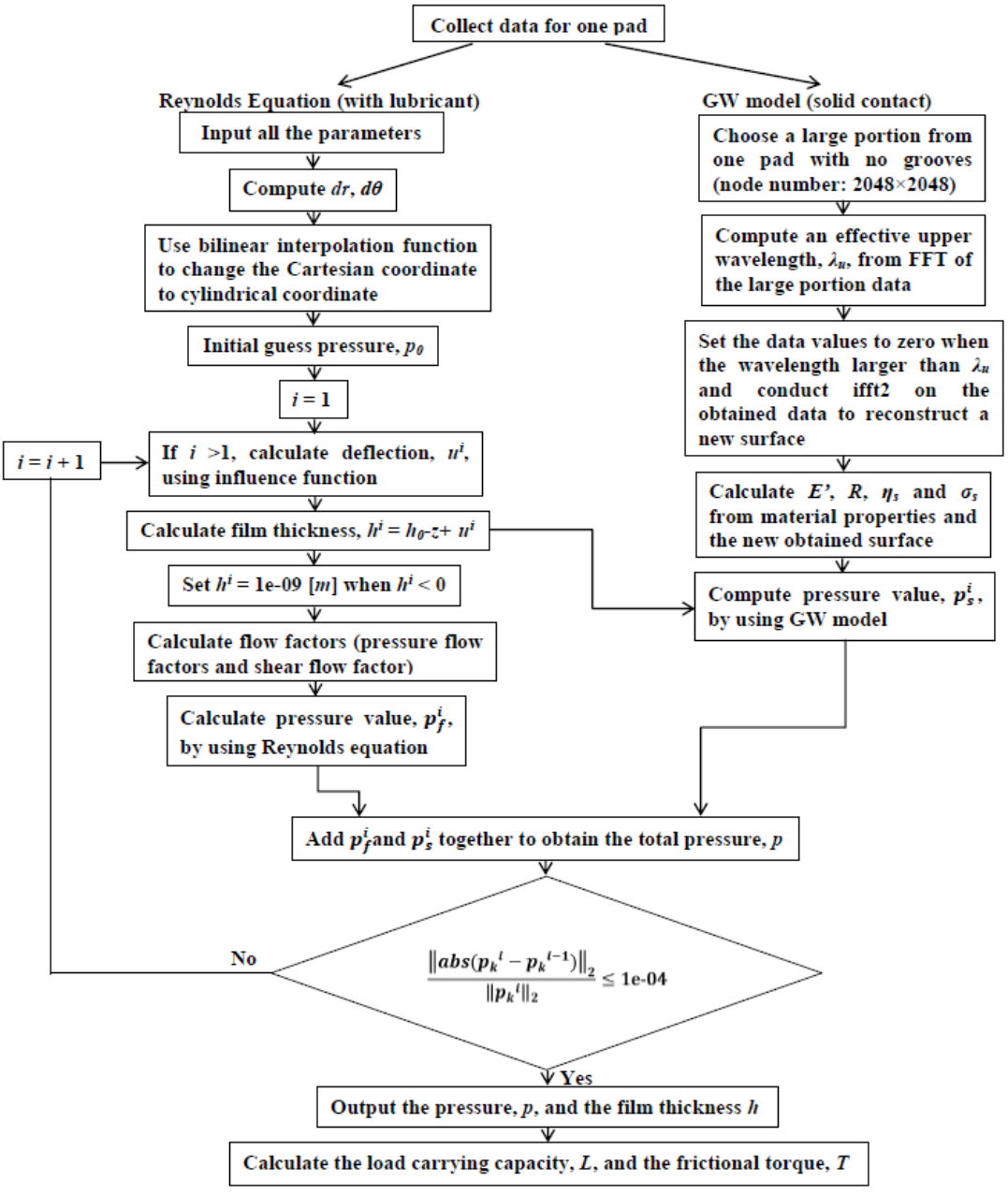

Fig.2 - Flow chart of the mixed lubrication analysis

As we discussed in the references [18, 19], the roughness-length method appears to be the most effective and reliable method in calculating the fractal dimension, so the 3D roughness-length

method [20] is used to calculate the fractal dimension of the measured thrust washer surface in this work. The roughness here is described by the standard deviation. For the 3D rough surfaces, the power law relationship between $S(w)$ (the standard deviation of the surface height) and w (the sampling length window size) can be calculated by the equation below [20]:

$$S(w) = Aw^H \tag{6}$$

where H is the Hurst exponent and A is a constant defined as a measure of amplitude of a profile (amplitude parameter). By dividing the rough surface into a grid of squares with the window length w, $S(w)$, which can also be regarded as the root-mean-square roughness of the divided squares, and can be calculated according to the following equation [20]:

$$S(w) = RMS(w) = \frac{1}{n_w}\sum_{i=1}^{n_w}\sqrt{\frac{1}{m_i - 2}\sum_{j\in w_i}(z_j - \bar{z})^2} \tag{7}$$

where n_w is the total number of square windows with the side length, w; m_i is the total number of points in the square window, w_i; z_j is the residuals of the asperity height on the trend, and $\bar{z}$ is the mean residual asperity height in each square window. For surfaces, the Hurst exponent, H, is related to the fractal dimension, D, with the equation $D = 3\text{-}H$. H can be obtained from the slope of the log-log plot of $S(w)$ and w.

Thrust bearing model

In our model, a polymer thrust bearing surface is scanned with a Bruker NPFLEX system. The scanned thrust bearing surface is shown in Fig.3(a) (the coordinate values are normalized by the outer radius value of the thrust bearing (r_o)). The rough surface of a single pad with 2048×2048 nodes is chosen from this thrust bearing surface as shown in Fig.3(b) (the coordinate values are normalized by the outer radius value of the thrust bearing (r_o)), and the surface data is leveled to make sure the average slope of the surface is zero before calculating the surface parameters. The

reason we choose 2048×2048 nodes on the measured surface is that the Fast Fourier transform (FFT) method will be used in the analysis, it is the most efficient when the number of samples is a power of 2. In addition, other common statistical parameters, like root mean square roughness (σ), skewness (Sk) and kurtosis (K), are also calculated based on [21 - 23] and listed in Table 1. The fractal dimension value of the measured rough surface is calculated by the roughness-length method [15]. The calculated fractal dimension value is also listed in Table 1.

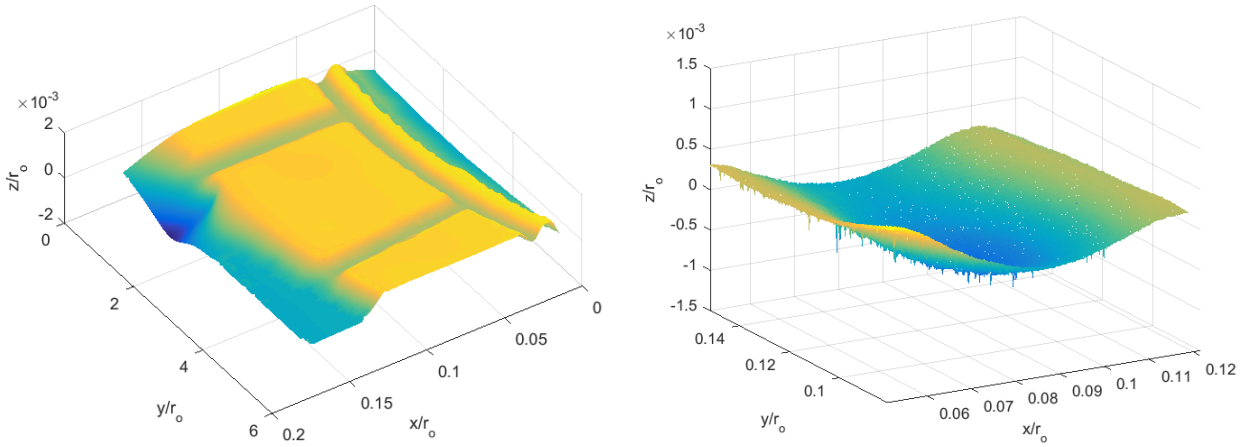

(a) (b)

Fig.3 - Scanned thrust bearing surface and the chosen rough surface. Shown are (a) scanned thrust bearing surface; (b) rough surface with 2048×2048 nodes from thrust bearing

The surface data is measured in Cartesian coordinates, while the Reynolds equation used is in the cylindrical coordinates (see Eq.(1)) because the thrust bearing geometry is annular. Therefore, a coordinate transformation is performed. When the collected surface data is used in the Reynolds equation to calculate the fluid pressure, they are mapped back onto the cylindrical coordinate, so that the nodes match the geometry of the bearing. A bilinear interpolation is used for the coordinate transformation.

After the thrust bearing surface data are collected, the surface is deconstructed into small scale roughness and large scale roughness via a filtering algorithm according to a cut-off frequency (a frequency equals to the reciprocal of a specific cut-off wavelength of the rough surface). The parameters

of the rough surface contact and the flow factors can be calculated according to the small scale roughness. Fig.4 shows the process of surface deconstruction. By combining the small scale roughness part via rough surface contact and flow factors and the large scale geometry part from Reynolds equation and bulk deflection together, our bearing model is formed.

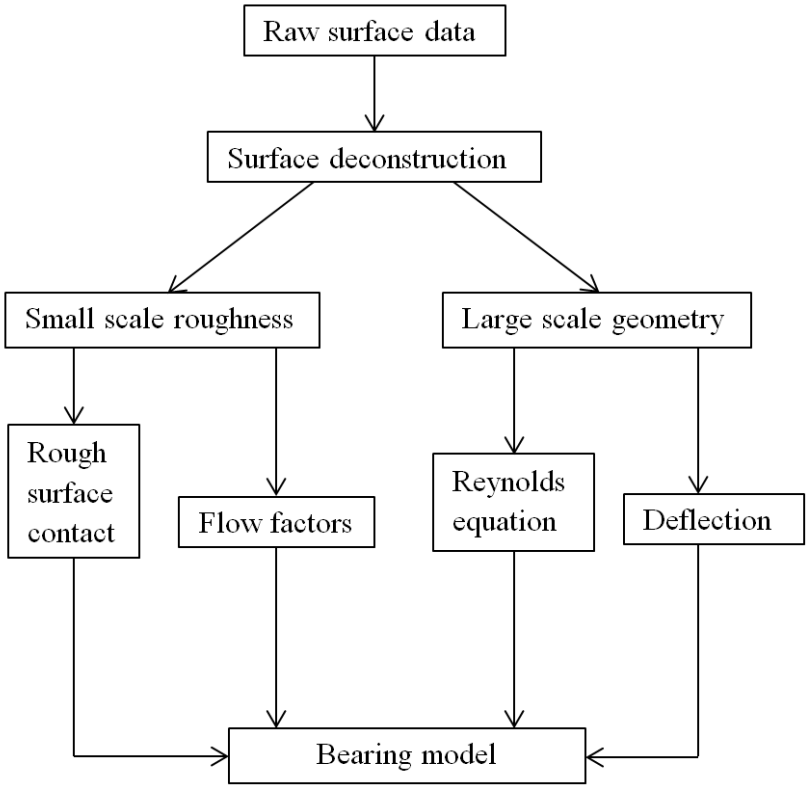

Fig.4- Process of surface deconstruction

The bulk deflection of a node on the surface in the large scale geometry part induced by an arbitrary pressure distribution in our work is calculated by using the influence coefficient method [24]:

$$(u_{ij})_m = \sum_{k=1}^{N}\sum_{l=1}^{M} k_{ijkl} \cdot p_{kl} \tag{8}$$

where $(u_{ij})_m$ is the bulk deflection of the calculated point, k_{ijkl} is the influence coefficient， it is only valid for half-space which is only an approximation to the normal deflection of an annular shaped washer, p is the uniform pressure applied on the discrete points of the surface.

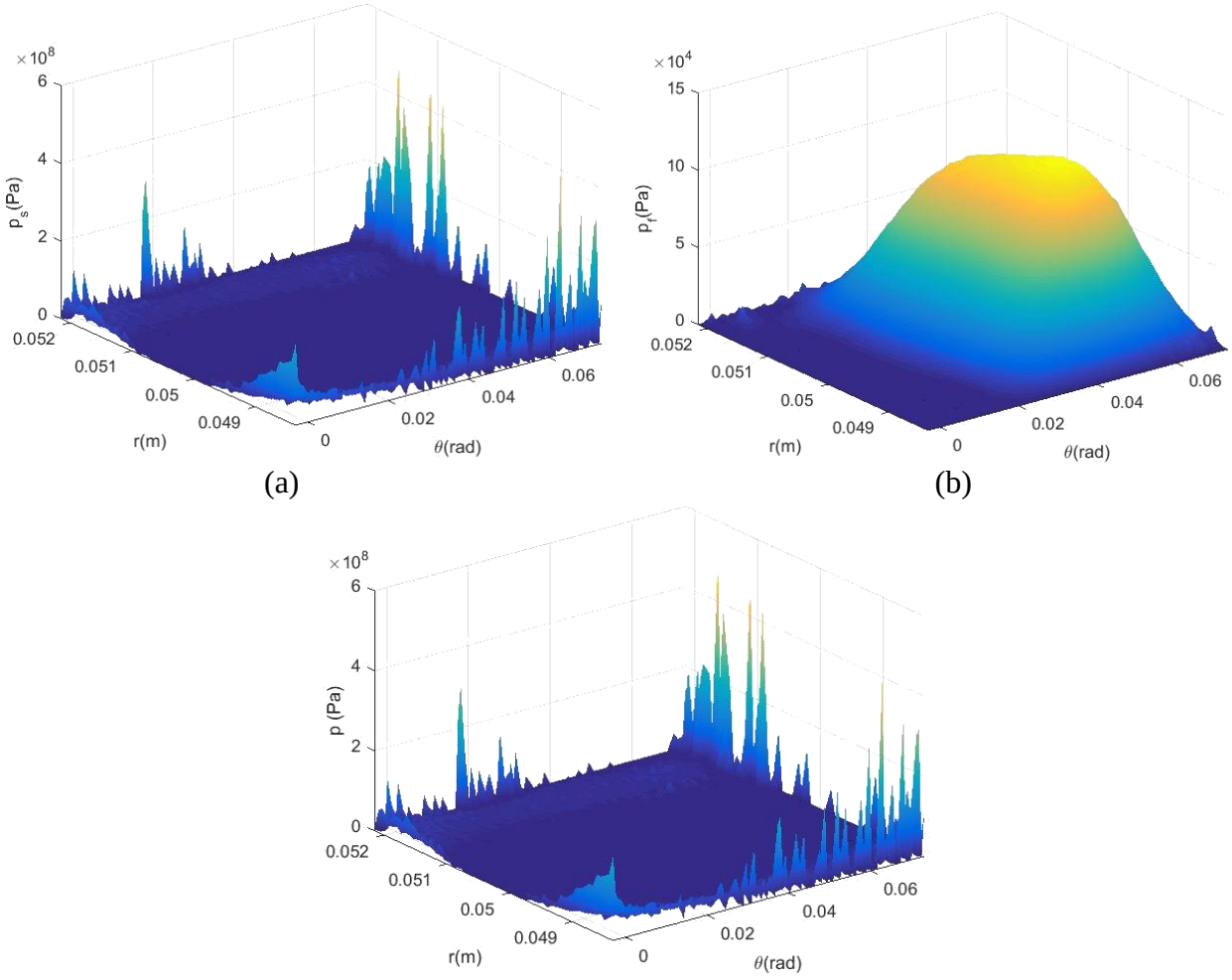

Fig.5 - Pressure distribution on the thrust bearing (f_c = 33,300 m^{-1}, h_0 = 1 μm, ω = 0.14 *rad/s*). Shown are the (a) solid contact pressure distribution; (b) fluid pressure distribution; (c) total pressure distribution

According to Eq. (1) and Eq. (4), the fluid pressure and solid contact pressure can be calculated, and then the total pressure on the thrust bearing can be obtained by adding them together. The solid contact pressure distribution, the fluid pressure distribution and the total pressure distribution for a specific case are shown in Fig.5. In this specific case, the cut-off

frequency is f_c = 33,300 m^{-1}(the wavelength, λ, is 30 μm), the initial surface separation is h_0 = 1 μm and the angular velocity (the velocity of the thrust bearing rotated around the intermediate shaft) based on an application of this bearing is ω = 0.14 *rad/s*. After the pressure and shear stress are obtained, the torque and load carrying capacity of the thrust bearing can be calculated.

Surface Generation

Two different methods are used to artificially generate rough surfaces with the same fractal dimension, *D*, calculated from the measured rough surface. One is the 3D PSD-iFFT method (the inverse Fourier transform based on a prescribed Power Spectral Density). The other one is the midpoint displacement method, which can be abbreviated as MDM. The fractal dimension value used to generate the surface is 2.23, and is from the complete surface.

a) 3D PSD-iFFT method

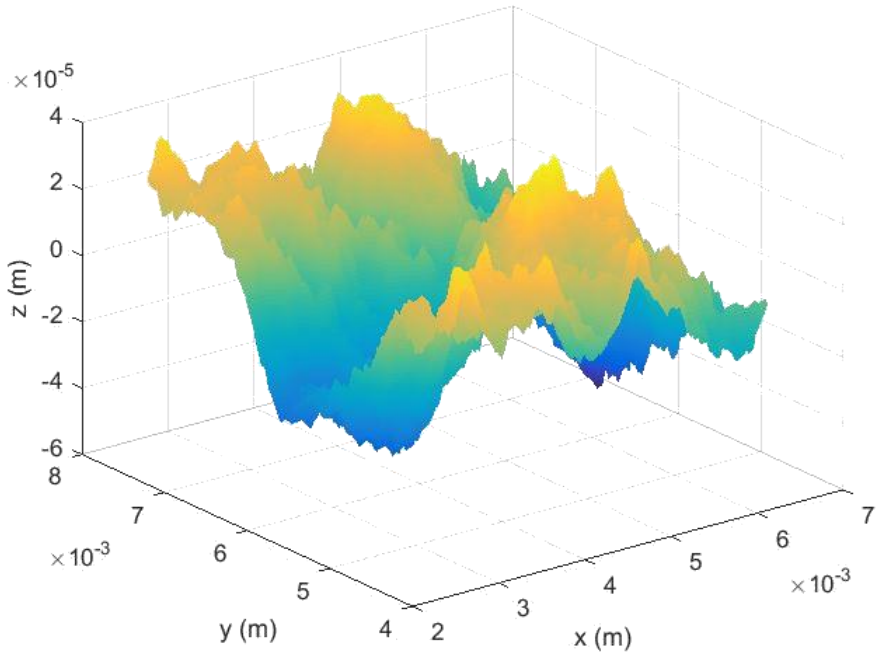

Fig.6 - Surface generated by using Eq. (9)

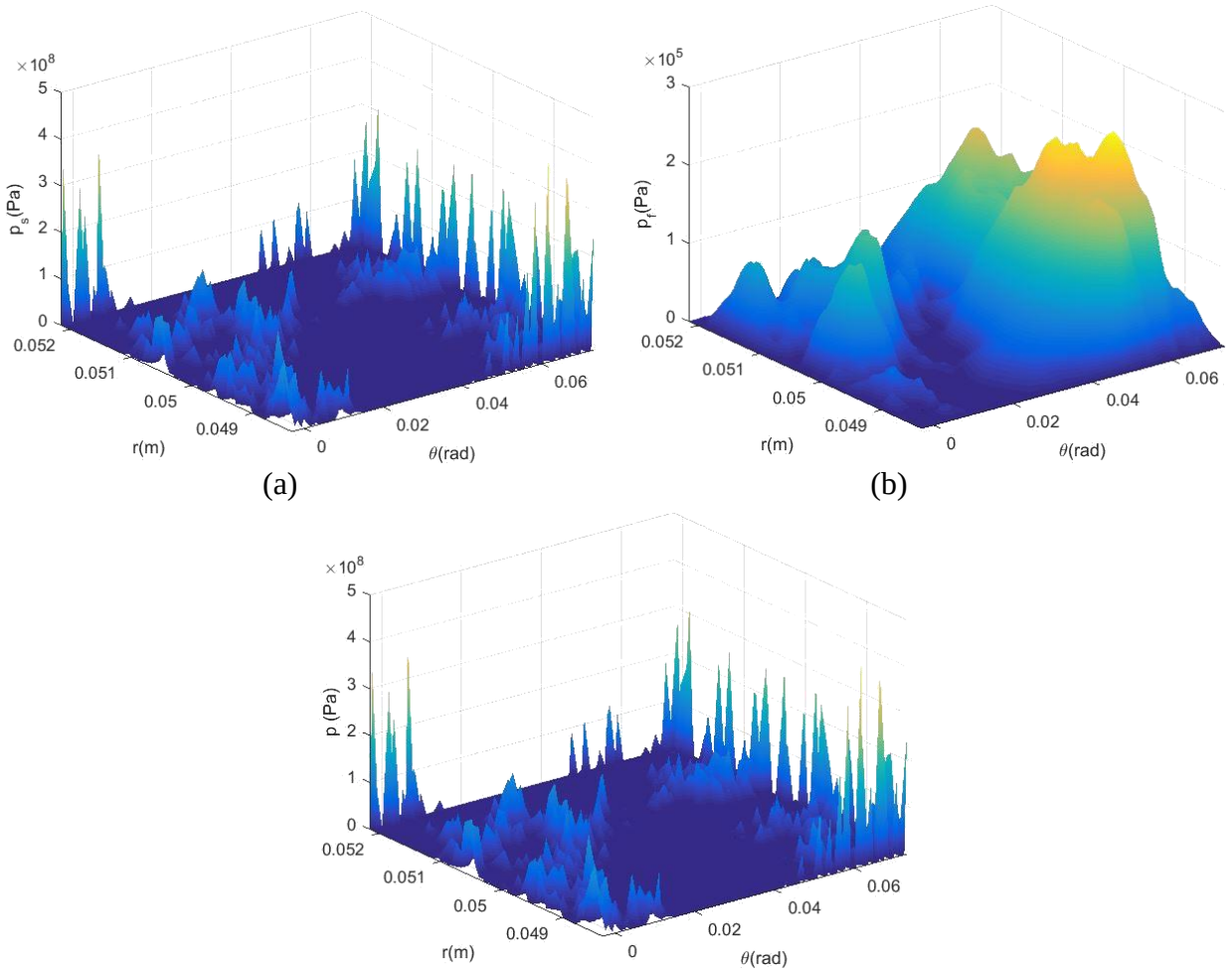

Fig.7 - Pressure distribution on the PSD generated surface (f_c = 33,300 m^{-1}, h_0 = 1 μm, ω = 0.14 *rad/s*). Shown are the (a) solid contact pressure distribution; (b) fluid pressure distribution; (c) total pressure distribution.

According to Yastrobov [25] and Putignano [26], the surface topographies $z(x,y)$ can be generated with a power spectral density, which is calculated by Eq. (9).

$$C(q) = C_0 \left(\frac{q}{q_0}\right)^{-2(1+H)} \tag{9}$$

$$q_0 = \frac{2\pi}{L} \tag{10}$$

$$q = \sqrt{q_x^2 + q_y^2} \tag{11}$$

where C_0 is a constant, q_0 is the cut-off wave vector, L is the length of the measured surface, q_x and q_y are frequencies in x and y direction. After the power spectral density (PSD) is calculated by Eq. (9), the surface can be generated by applying the Hermitian symmetry and the inverse Fourier transform on the obtained PSD (which is shown in Fig.6). The same mapping process and the surface deconstruction process are conducted on this PSD generated surface. Some basic parameters and the fractal dimension value calculated by the roughness-length method [20] for the PSD generated surface are also listed in Table 1.

Fig.7 shows the solid contact pressure distribution, the fluid pressure distribution and the total pressure distribution of the PSD generated surface based on Eq.(1) and Eq.(4) for the same specific case as the measured surface. Then the load carrying capacity and the torque values for the PSD generated surface computed based on the total pressure and shear stress can be calculated.

b) Midpoint displacement method

This surface generation method was first proposed by Fournier et. al.[27] in 1982 and then discussed by Saupe [28] and Voss [29]. The generated process of this method can be summarized below:

1) Considering a square in the x-y plane, the height of four corners in the plane is from the Gaussian distribution $N(\mu, \sigma^2)$;

2) Picking up the midpoint of the square, the height of the midpoint is the average value of the four corners plus a Gaussian random number $N(0,1)$. Meanwhile, the RMS roughness, σ_i, in the i-th iteration need to be modified according to the fractal dimension value is calculated from the measured surface;

3) Calculating the height of midpoint in every side of the square, then the initial plane can be divided into four new squares;

4) This process is repeated for each new obtained square until we get the desired surface resolution.

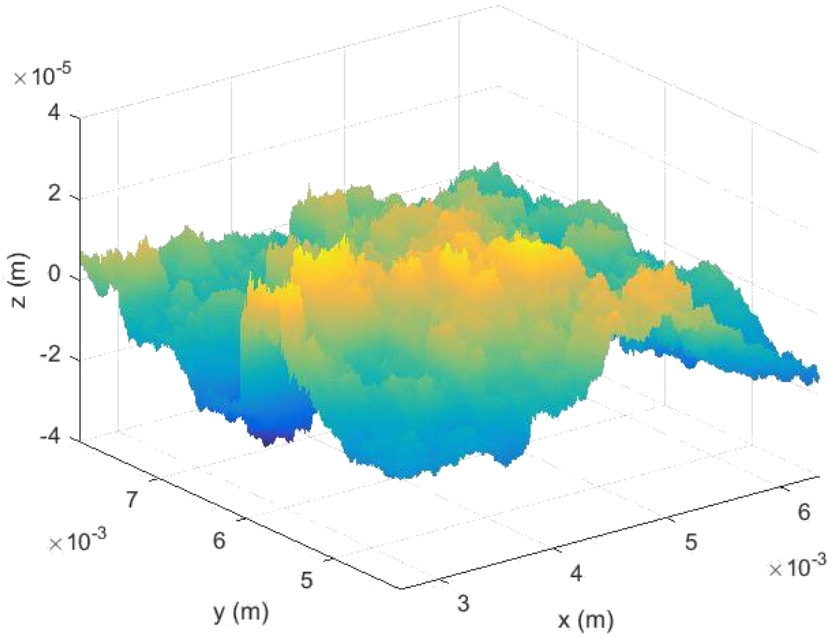

Fig.8 - Surface generated by midpoint displacement method

Table 1 - Basic parameters calculated for the measured surface, the PSD generated surface and the MDM generated surface

Parameters	Measured surface	PSD generated surface	MDM generated surface
Root mean square (σ)	$1.1074\times10^{-5}\ m$	$1.2619e\times10^{-5}\ m$	$7.0002\times10^{-6}\ m$
Kurtosis (K)	2.8980	7.2189	4.7459
Skewness (Sk)	0.0908	-1.0941	0.0768
Asperity radius (R)	$1.1096\times10^{-5}\ m$	$1.2370\times10^{-5}\ m$	$4.6311\times10^{-6}\ m$
Asperity density (η_s)	$3.5170\times10^{10}\ m^{-2}$	$2.6728e\times10^{10}\ m^{-2}$	$7.9589\times10^{10}\ m^{-2}$
Fractal dimension (D)	2.23	2.23	2.11

Fig.8 shows the surface generated from the midpoint displacement method (MDM). The same parameters are calculated for the MDM generated surface and listed in Table 1. Again, the same mapping process and the surface deconstruction process are conducted on this MDM generated surface.

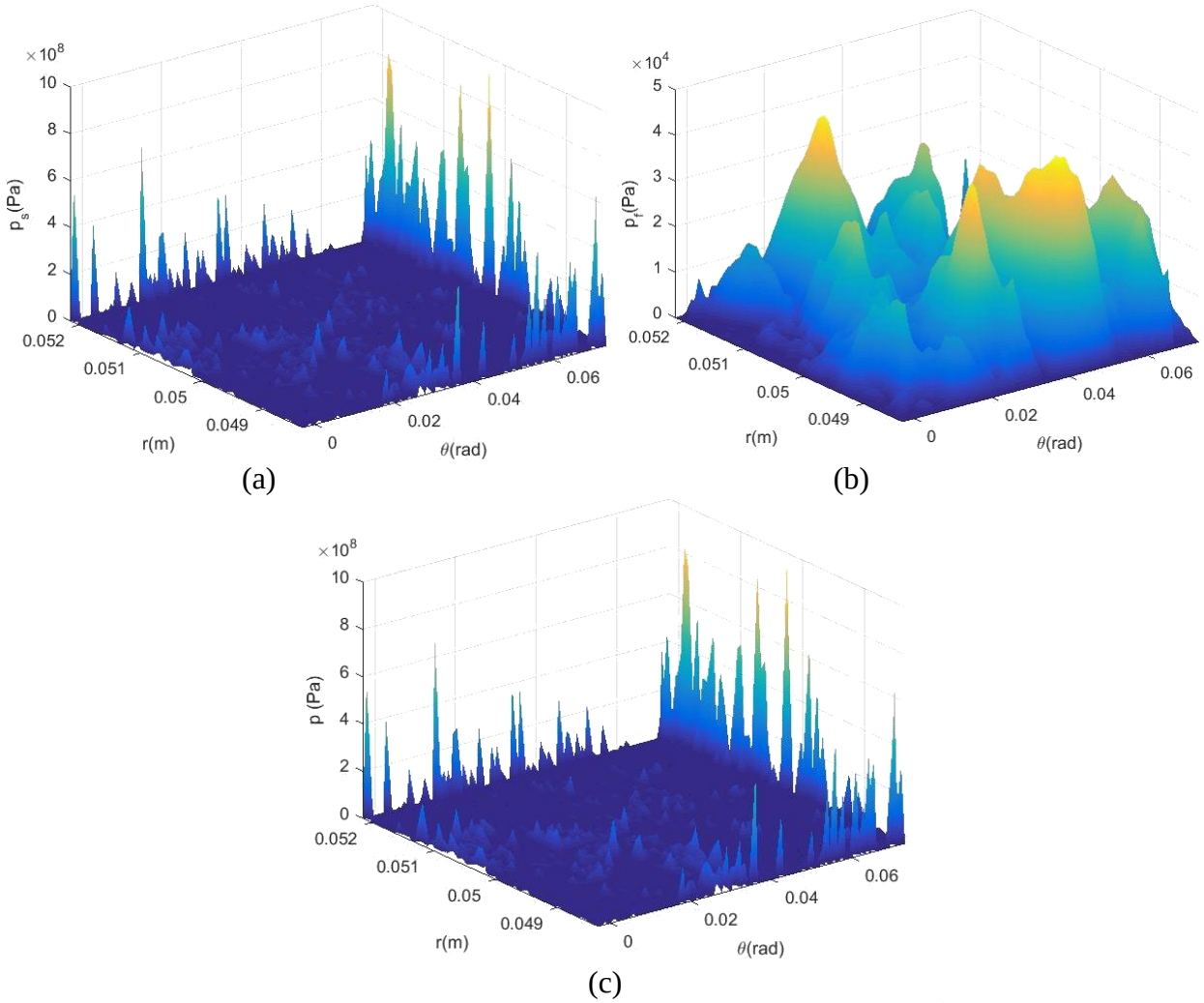

Fig.9 - Pressure distribution on the MDM generated surface (f_c = 33,300 m^{-1}, h_0 = 1 μm, ω = 0.14 *rad/s*). Shown are the (a) solid contact pressure distribution; (b) fluid pressure distribution; (c) total pressure distribution

In the MDM process, the expectation of the distribution, μ, and root mean square roughness, σ, values are all from the measured surface shown in Fig.3(b). Since the fractal dimension value D = 3-H, the fractal dimension value in step 2) is considered by using the equation below [30]:

$$\sigma_i^2 = \frac{1}{2^{2H(i+1)}}\sigma^2 \tag{12}$$

where σ_i is a modified RMS roughness in the *i-th* iteration of the method.

The solid contact pressure distribution, the fluid pressure distribution and the total pressure distribution of the MDM generated surface based on the same specific case as the measured surface

are calculated and plotted in Fig.9. The load carrying capacity and the torque values then can be computed for the MDM generated surface.

Results and Discussions

It can be found from Fig.5, Fig.7 and Fig.9 that the pressure contribution from the fluid is very small compared to the values from solid contact, so that the contribution of load carrying capacity from fluid is also very small for this application case. As we mentioned previously, these cases are for a relatively low angular velocity of 0.14 *rad/s* based on the actual application of this bearing. Therefore, the influence of angular velocity at values larger than this on the load carrying capacity and the torque are also investigated. With the constant cut-off frequency (f_c = 33,300 m^{-1}) and the same initial surface separation (h_0 = 1 μm), the angular velocity is changed from 0.14 *rad/s* to 419 *rad/s*. Figs. 10(a) and 11(a) show the relationships between the total load carrying capacity (L_{total}) and the total torque (T_{total}) as a function of the angular velocity (ω) for these three surfaces. The changing trends of the ratio for the contribution of the fluid part and the solid contact part on the load carrying capacity and the torque with the changing of the angular velocity (ω) for these three surfaces are shown in Figs. 10(b) and 11(b).

Fig.10(a) indicates that with the increase of the angular velocity, the load carrying capacity increases, which is in agreement with typical hydrodynamic bearing behavior. Again note that the original surface separation is held constant, but the actual surface separation can increase due to deformation. The slope of the load carrying capacity with speed is the steepest for the PSD generated surface, while it is the least for the measured surface. Meanwhile, for the same angular velocity, the load carrying capacity value from the PSD generated surface is larger than the other two surfaces when the angular velocity is larger than 20 *rad/s*.

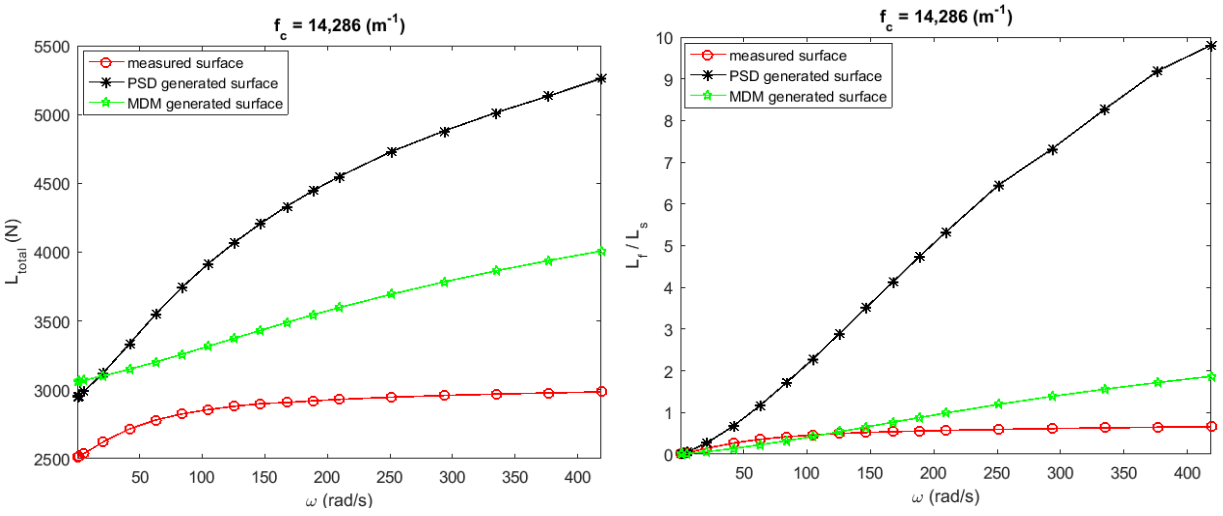

(a) (b)

Fig.10 - Influence of the angular velocity on the load carrying capacity. Shown are (a) relationship between the total load carrying capacity (L_{total}) and the angular velocity (ω); (b) relationship between the ratio of the load carrying capacity from the fluid part (L_f) and the load carrying capacity from the solid contact part (L_s) and the angular velocity (ω)

The proportion of the load carrying capacity also increases with the growth of the angular velocity, which means that the proportion of the load carrying capacity from the fluid has become significant. The ratio for the MDM generated surface is the smallest at the low angular velocity, but the ratio (L_f/L_s) from the measured surface becomes the smallest when the angular velocity becomes much larger. It should also be noted from Fig.10(b) that the ratio (L_f/L_s) for the measured surface is not larger than one, but the ratio (L_f/L_s) for the other two generated surfaces all become larger than one with the increase of the angular velocity. It means much of the load is carried more by the fluid if the ratio (L_f/L_s) is larger than one. This is more desirable for a typical fluid-film bearing. This may be due to clear differences in the larger scale geometries of the generated surfaces compared to the measured surface.

The same phenomena have also been predicted for the torque according to Fig.11. The torque values from these three surfaces increase with the increase of the angular velocity, the measured surface increases the most, while the PSD generated surface is the least. The contribution

of the torque from the fluid has increased with the growth of the angular velocity for these three surfaces.

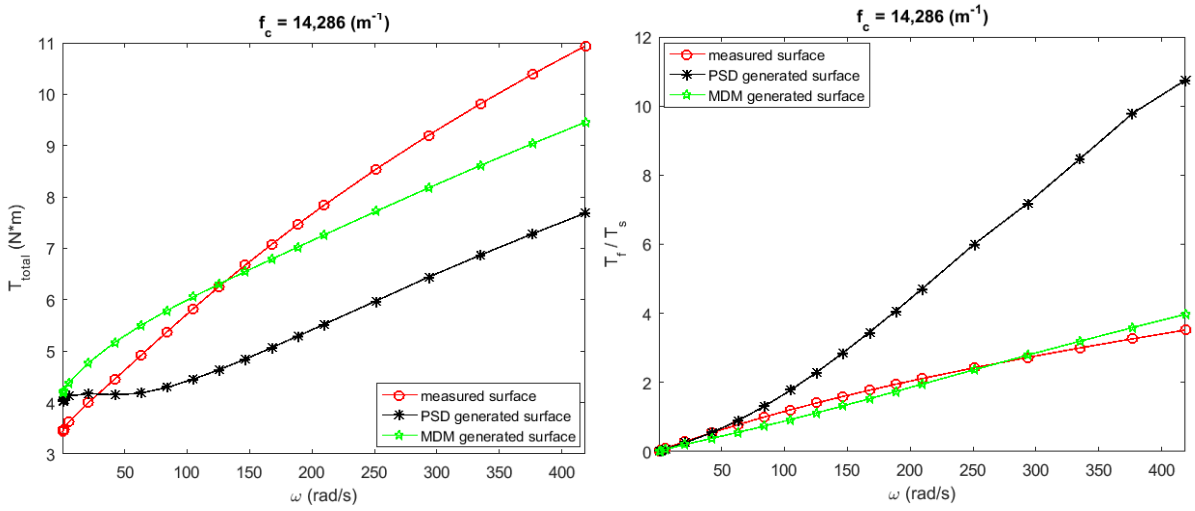

(a) (b)

Fig.11 - Influence of the angular velocity on the torque; Shown are (a) relationship between the total torque (T_{total}) and the angular velocity (ω); (b) relationship between the ratio of the torque from the fluid part (T_f) and the torque from the solid contact part (T_s) and the angular velocity (ω)

The ratios (L_f/L_s and T_f/T_s) from the PSD generated surface is the largest for all cases. The proportion of the load carrying capacity and the torque from the fluid increases significantly with the growth of the angular velocity and becomes much larger than the load carrying capacity and the torque from solid contact for the PSD generated surface. The increase of the ratios (L_f/L_s and T_f/T_s) with the angular velocity for the measured surface and the MDM generated surface is much less. The ratios (L_f/L_s and T_f/T_s) from the measured surface becomes the smallest gradually, which means the contact area in the measured surface is larger than the contact area in the other two generated surfaces at the same angular velocity.

It can be concluded from the analysis above that the angular velocity has a different influence on the two generated surfaces from the measured surface. Therefore, the two surface generation methods are not suitable in representing the measured surface.

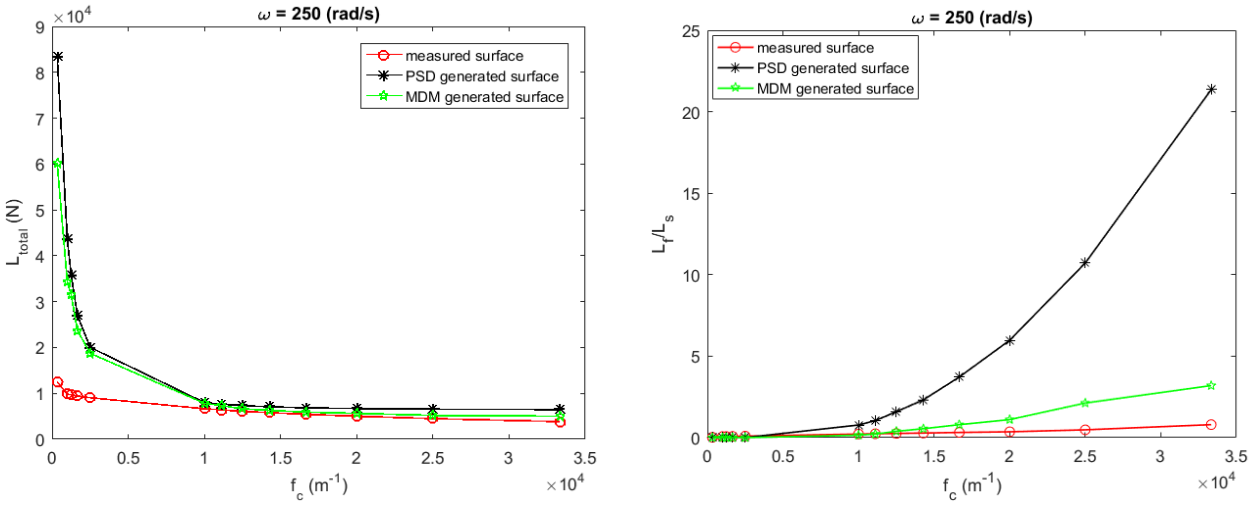

(a) (b)

Fig.12 - Influence of the cut-off frequency on the load carrying capacity. Shown are (a) relationship between the total load carrying capacity (L_{total}) and the cut-off frequency (f_c); (b) relationship between the ratio of the load carrying capacity from the fluid part (L_f) and the load carrying capacity from the solid contact part (L_s) and the cut-off frequency (f_c)

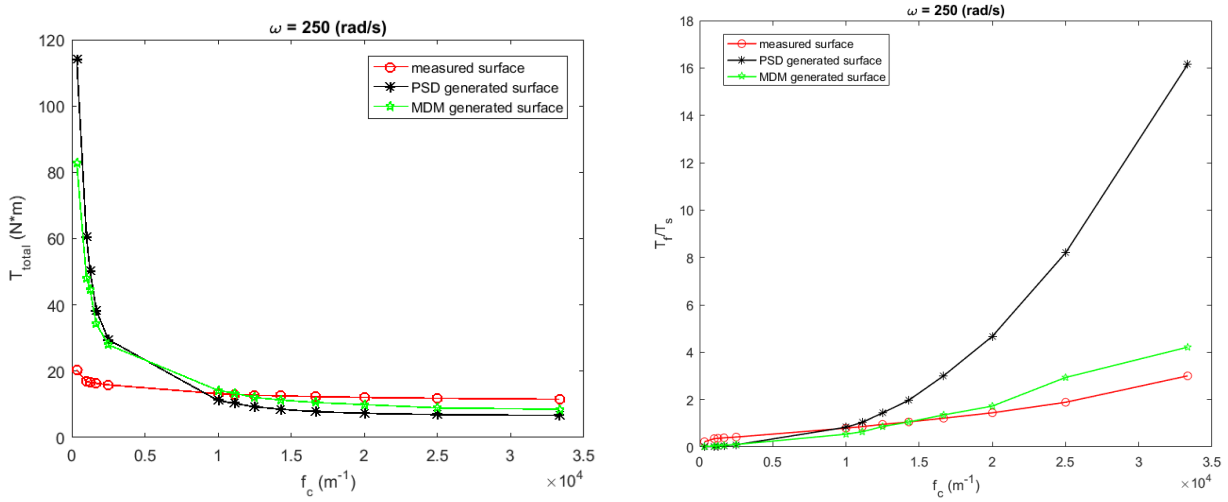

(a) (b)

Fig.13 - Influence of the cut-off frequency on the torque; Shown are (a) relationship between the total torque (T_{total}) and the cut-off frequency (f_c); (b) relationship between the ratio of the torque from the fluid part (T_f) and the torque from the solid contact part (T_s) and the cut-off frequency (f_c)

In the case we discussed above, the cut-off frequency we used to deconstruct the surface is f_c = 33,300 m^{-1}. More cases with different cut-off frequencies (changing from 333 m^{-1} to 33,300 m^{-1}) are run for these three different surfaces (the angular velocity is held constant during this process

at ω = 250 *rad/s* and the initial surface separation is h_0 = 1 μm), and the plots of the influence of the cut-off frequency on the load carrying capacity and the torque for these three surfaces are shown in Figs. 12 and 13. Note that as the cut-off frequency is increased, more of geometry is included deterministically in the model rather than by using the Greenwood & Williamson (GW) model [14] and Patir and Cheng roughness model [12, 13].

It can be seen from Figs. 12(a) and 13(a) that the total load carrying capacity value and the total torque value from the two generated surfaces are very large when the cut-off frequency is very small. Whereas, the total load carrying capacity value and the total torque value from two generated surfaces decrease with the increase of the cut-off frequency. Meanwhile, the predictions of these two values from two generated surfaces become coincident with the values for the measured surface if the cut-off frequency becomes large enough. The total load carrying capacity and the total torque values from the MDM generated surface are much closer to the values from the measured surfaces than the PSD generated surface. It should also be noted that the change of the total load carrying capacity value and the total torque value from the measured surface is relatively small with the increase of the cut-off frequency. However, the points at the highest cut-off frequency (33,300 m^{-1}) are not in reasonable agreements, which is the same case shown in Fig.11.

In addition, Fig.12(b) shows the influence of the cut-off frequency on the ratio (L_f/L_s) of the load carrying capacity from the fluid part and the load carrying capacity from the solid contact part. The ratio (L_f/L_s) for all these three surfaces increases with the increase of the cut-off frequency, which means much of the load is carried by the fluid when the cut-off frequency becomes large. The slope of the increase speed of the ratio (L_f/L_s) from the PSD generated surface is the steepest compared with the measured surface and the MDM generated surface with the increase of the cut-

off frequency. The increase trend for the measured surface and the MDM generated surface is much closer. Same phenomena have happened for the influence of the cut-off frequency on the ratio (T_f/T_s) of the torque from the fluid part and the torque from the solid contact part shown in Fig.13(b).

From the analysis above, when the cut-off frequency used to deconstruct the surface is small, both of the PSD generated surface and the MDM generated surface are not very suitable in representing the measured surface. However, these two generated surfaces can represent the measured surface when the cut-off frequency becomes large and the MDM generated surface seems much more suitable in representing the measured surface compared with the PSD generated surface. It means that the characterization ability of the generated surfaces depends heavily on the cut-off frequency.

By comparing the parameter values in Table 1, the σ values of the measured surface, the PSD generated surface and the MDM generated surface have little difference between the surfaces. The *Sk* and *K* values for the MDM generated surface are much closer to the measured surface than the PSD generated surface, but the values of asperity radius, *R*, and asperity density, η_s, calculated from the MDM generated surface are not as consistent as the values calculated by the PSD generated surface when comparing with the values of the measured surface. Clearly, these two regenerated fractal surfaces are structured fundamentally different than the measured surface.

It should be noted that both of the two generated surface methods consider the fractal dimension value when generating the surface, and the generated surfaces based on these two methods are not very consistent in characterizing the measured surface. Therefore, it should be considered carefully if a generated surface based on the fractal dimension can be used to represent a measured surface. Since the differences of the predicted results, the fractal dimension is not a

reliable value to solely characterize the measured surface. However, if other parameters could be considered in the generated process as well, improvement might be made. In addition, since only a few generated surfaces are evaluated due to the computational limitations, the results cannot be considered generalized.

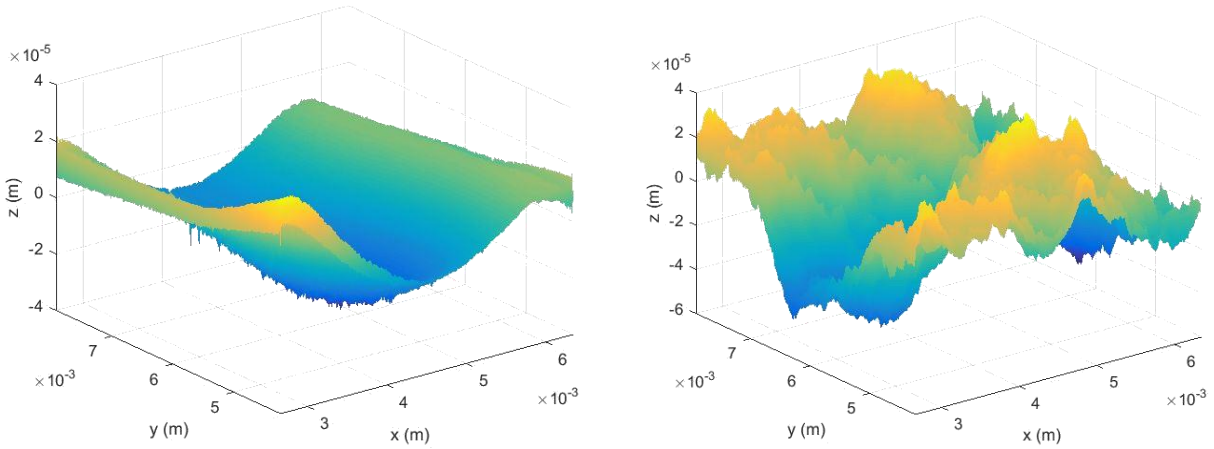

Surface A Surface B

Fig.14 - Two new generated surfaces based on the measured surface data and the PSD generated surface data

Meanwhile, two new surfaces (surface A and surface B) are also constructed based on the small scale roughness and the large scale roughness of the measured surface and the PSD generated surface using the following method (see Fig.14):

(1) Surface A: combine large scale roughness from the measured surface with small scale roughness from the PSD generated surface;

(2) Surface B: combine small scale roughness from the measured surface with large scale roughness from the PSD generated surface.

Small scale roughness and large scale roughness are determined based on the cut-off frequency. Surface A and surface B shown in Fig.14 are generated when the cut-off frequency is 33,300 m^{-1}. For these two shown surfaces, the same basic parameters and the fractal dimension value from the roughness-length method [20] are calculated (see Table 2).

The measured surface and surface A have similar values of σ, Sk and K, and the values of σ, Sk and K for the PSD generated surface and surface B are similar based on Table 1 and Table 2, which means large scale roughness tends to dominate the calculation process of the statistical parameters.

Table 2 - Related parameters calculated for surface A and surface B

	Surface A	Surface B
Root mean square (σ)	1.1063×10^{-5} m	1.2617×10^{-5} m
Kurtosis (K)	2.9026	7.2077
Skewness (Sk)	0.0941	-1.0911
Asperity radius (R)	1.2375×10^{-5} m	1.1096×10^{-5} m
Asperity density (η_s)	2.6728×10^{10} m^{-2}	$3.5170e\times10^{10}$ m^{-2}
Fractal dimension (D)	2.51	2.16

In addition, it is important to understand the physical meaning of different values of the fractal dimension when discussing the results. According to Majumdar and Bhushan [8], the surface fractal dimension (D_s) can be related to the profile fractal dimension (D_p) by using $D_s = 1+D_p$. Self-affinity defines a geometry that repeats over many scales for which the scaling ratio are not the same in different directions, while the scaling ratio for a self-similar object is the same in all directions. It has already been proven in our previous work [18, 19] that the fractal dimension value for a self-similar surface profile is 1. Therefore, the fractal dimension for a self-similar surface should be 2. Note that a surface profile is one line of a 3-D surface.

Table 3 - Some parameters calculated based on different cut-off frequencies

	surface A				surface B			
f_c (m^{-1})	σ (m)	Sk	K	D	σ (m)	Sk	K	D
50,000	1.1067×10^{-5}	0.0939	2.9026	2.5895	1.2619×10^{-5}	-1.0917	7.2096	2.3775
33,300	1.1063×10^{-5}	0.0941	2.9026	2.5074	1.2617×10^{-5}	-1.0911	7.2077	2.1587
25,000	1.1060×10^{-5}	0.0942	2.9030	2.4358	1.2615×10^{-5}	-1.0906	7.2059	2.1646

20,000	1.1057×10^{-5}	0.0944	2.9035	2.4127	1.2613×10^{-5}	-1.0902	7.2043	2.1400
16,700	1.1055×10^{-5}	0.0945	2.9037	2.3962	1.2610×10^{-5}	-1.0899	7.2028	2.1235
14,300	1.1053×10^{-5}	0.0945	2.9037	2.3713	1.2607×10^{-5}	-1.0897	7.2016	2.1134
12,500	1.1051×10^{-5}	0.0945	2.9039	2.3532	1.2604×10^{-5}	-1.0897	7.2017	2.1034
11,100	1.1049×10^{-5}	0.0944	2.9043	2.3414	1.2600×10^{-5}	-1.0894	7.2000	2.0810
10,000	1.1047×10^{-5}	0.0943	2.9045	2.3414	1.2596×10^{-5}	-1.0896	7.1997	2.0717
5000	1.1039×10^{-5}	0.0924	2.9065	2.3018	1.2547×10^{-5}	-1.0920	7.2059	2.0559
3330	1.1036×10^{-5}	0.0882	2.9008	2.2932	1.2485×10^{-5}	-1.0986	7.2266	2.0620
2500	1.1036×10^{-5}	0.0814	2.8894	2.2816	1.2411×10^{-5}	-1.1041	7.2697	2.0648
2000	1.1042×10^{-5}	0.0745	2.8700	2.2799	1.2324×10^{-5}	-1.1253	7.2823	2.0725
1670	1.1045×10^{-5}	0.0647	2.8484	2.2848	1.2235×10^{-5}	-1.1428	7.2957	2.0900
1430	1.1049×10^{-5}	0.0532	2.8149	2.2826	1.2090×10^{-5}	-1.1562	7.5180	2.1101
1250	1.1061×10^{-5}	0.0310	2.7518	2.2869	1.1898×10^{-5}	-1.2293	7.7008	2.1328
1110	1.1061×10^{-5}	0.0310	2.7518	2.2869	1.1898×10^{-5}	-1.2293	7.7008	2.1328
1000	1.1082×10^{-5}	-0.0035	2.6532	2.2870	1.1601×10^{-5}	-1.2700	7.8841	2.2058
500	1.1479×10^{-5}	-0.1753	2.7466	2.2768	8.9553×10^{-5}	-1.6790	11.685	2.2861
333	1.1479×10^{-5}	-0.1753	2.7466	2.2768	8.9553×10^{-5}	-1.6790	11.685	2.2861

By comparing the fractal dimension values in Table 1 and Table 2, it can be seen that the measured surface, the PSD generated surface, the MDM generated surface and surface B tend to be self-similar, but surface A tend to be self-affine. Nonetheless, the parameter values listed in Table 2 are based on the specific case (f_c = 33,300 m^{-1}), different cut-off frequencies are changed to verify the influence of cut-off frequency on some parameters listed in Table 2 and the values are listed in Table 3.

It can be found from Table 3 that values of σ, K and Sk for surface A and surface B do not change significantly along with the changing of the cut-off frequency, except at low cut-off frequencies, which are near to the macro scale geometry and would not typically be used. However, the fractal dimension value is influenced significantly by the changing of the cut-off frequency.

Fig.15 shows the relationship between the cut-off frequency and the parameter values for surface A and surface B based on Table 3.

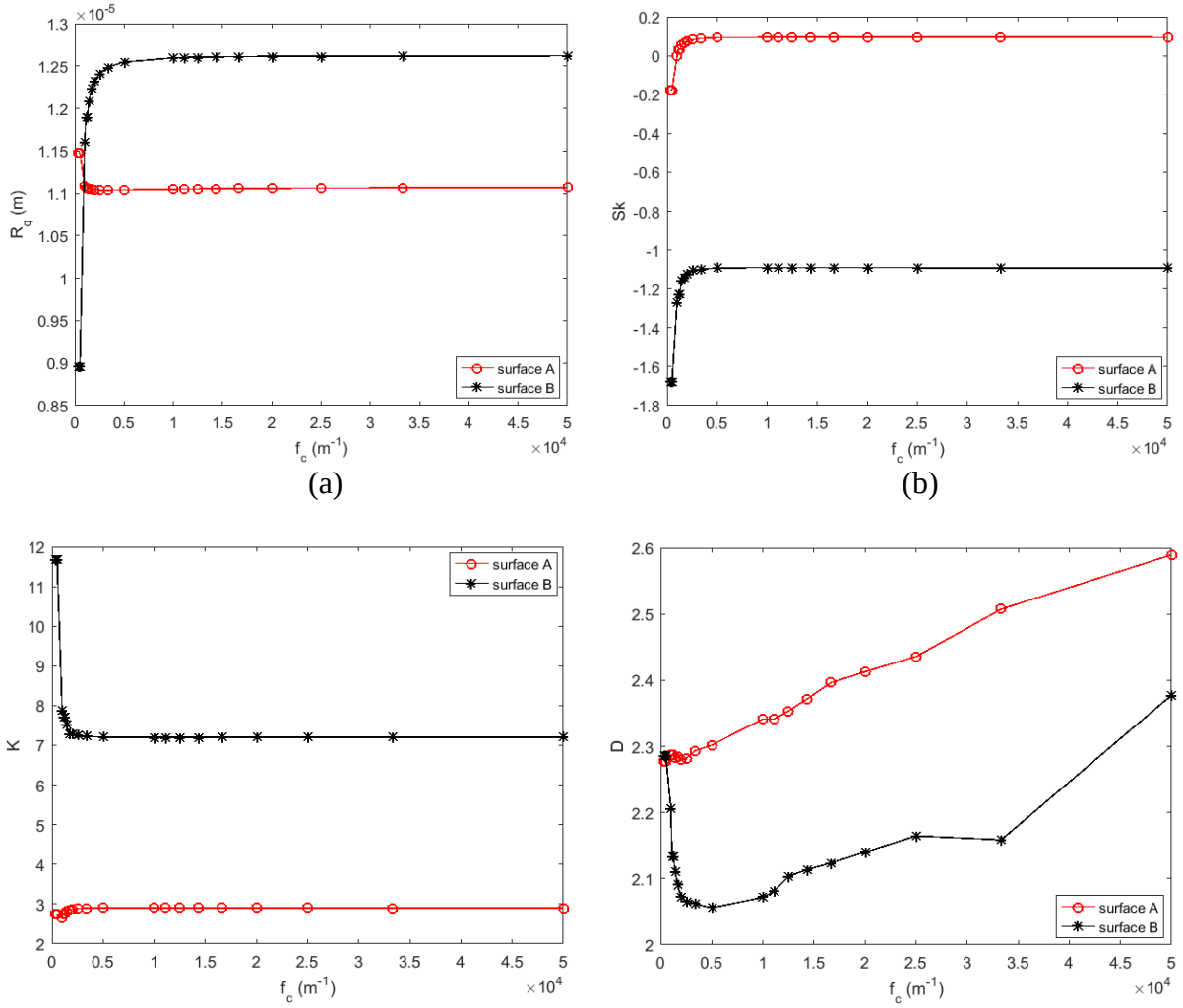

Fig.15 - Relationship between the cut-off frequency and the parameter values in Table 3

According to Fig.15 (a), (b), and (c), the values of σ, Sk and K do not have significantly change when the cut-off frequency becomes larger, though these three values have changed at the lower cut-off frequency. For the relationship between the cut-off frequency and the fractal dimension shown in Fig.15(d), fluctuation happens in the fractal dimension value with the increase of the cut-off frequency. It can be concluded that fractal dimension, D, actually varies more than roughness or statistical values with scale, which means that the fractal dimension depends on the

chosen cut-off frequency and it is not always a reliable parameter in characterizing the rough surface.

Conclusions

In this work, a mixed lubrication bearing model is proposed and used to evaluate different realizations of the same surface. With the increase of the angular velocity, the load carrying capacity and the torque values from the real surface, the PSD generated surface and the MDM generated surface all increase, but at different amounts. The proportions of the load carrying capacity and the torque from fluid have also increased for the measured surface, the PSD generated surface and the MDM generated surface with the growth of the angular velocity. However, the ratios (L_f/L_s and T_f/T_s) from the PSD generated surface has been the largest for all angular velocities and the ratios (L_f/L_s and T_f/T_s) from the measured surface becomes the smallest for larger angular velocities. Therefore, when the angular velocity increases large enough, the contact area of the measured surface is larger than the other two generated surfaces at the same angular velocity value. This suggests that the angular velocity has a greater influence on the two generated surfaces and that the two generated surfaces are not suitable in representing the measured surface.

When the cut-off frequency used in deconstructing the surface is small, the load carrying capacity value and the torque value from the PSD generated surface and the MDM generated surface are much larger than the values from the measured surface. Whereas, when the cut-off frequency becomes larger, the values of the load carrying capacity and the torque decrease and become closer to the values from the measured surface. Meanwhile, the MDM generated surface is relatively better in representing the measured surface than the PSD generated surface. It can be concluded that the cut-off frequency also has different influences on the two generated surfaces

from the measured surface and these two generated surfaces should be considered carefully in representing the measured surface.

The load carrying capacity value and the torque value calculated for the measured surface, the PSD generated surface and the MDM generated surface are not the same and the load carrying capacity ratio from the fluid and from solid contact for these three surfaces increases differently, which means it should be considered carefully whether the generated surface based on the fractal dimension can be used to represent a measured surface. It should be mentioned again that only a few generated surfaces are evaluated due to the computational limitations, therefore the results cannot be considered generalized.

Meanwhile, this work suggests that the fractal dimension is unreliable when it is the only parameter used to characterize the measured surface, since the results for the fractal surface and the measured surface differ significantly and it also changes with the chosen angular velocity and the cut-off frequency. Even considering the RMS roughness does to appear to resolve this issue. It should also be noted that large scale roughness appears to dominate the calculation process of the statistical parameters.

Although the input parameters for the generation rough surfaces are from the measured rough surface, some surface properties changed during the generation procedure, which implies that the surface generation methods we used in our work needs to be improved and new methods need to be developed.

References

[1] Yu TH, Sadeghi S. Groove Effects on Thrust Washer Lubrication. ASME J Tribol 2000; 123: 295-304.

[2] Jackson RL, Green I. Study of the Tribological Behavior of a Thrust bearing. Tribol Trans 2001; 44: 504-508.

[3] Taniguchi S, Ettles C. A Thermo-Elastic Analysis of the Parallel Surface Thrust Washer. ASLE Trans 1976; 18: 299-305.

[4] Jackson RL, Green I. The Thermoelastic Behavior of Thrust bearings Considering Mixed Lubrication Asperity Contact and Thermoviscous Effects. Tribol Trans 2008; 51: 19-32.

[5] Yu TH, Sadeghi S. Thermal Effects in Thrust Washer Lubrication. ASME J Tribol 2001; 124: 166-177.

[6] Jackson RL, Green I. The Behavior of Thrust bearings Considering Mixed Lubrication and Asperity Contact. Tribol Trans 2006; 49: 233-247.

[7] Majumdar A, Bhushan B. Role of Fractal Geometry in Roughness Characterization and Contact Mechanics of Surfaces. ASME J Tribol 1990; 112: 205-216.

[8] Majumdar A, Bhushan B. Fractal Model of Elastic-plastic Contact Between Rough Surfaces. ASME J Tribol 1991; 113: 1-11.

[9] Morag Y, Etsion I. Resolving the Contradiction of Asperities Plastic to Elastic Mode Transition in Current Contact Models of Fractal Rough Surfaces. Wear 2007; 262:624-629.

[10] Ge S, Tonder K. The Fractal Behavior and Fractal Characterization of Rough Surfaces. Tribology 1997; 17: 73-80.

[11] Mandelbrot BB, The Fractal Geometry of Nature. 1st ed. New York: W. H. Freeman and Company, 1982.

[12] Patir N, Cheng HS. An Average Flow Model for Determining Effects of Three-Dimensional Roughness on Partial Hydrodynamic Lubrication. ASME J Tribol 1978; 100: 12-17.

[13] Patir N, Cheng HS. Application of Average Flow Model to Lubrication Between Rough Sliding Surfaces. ASME J Tribol 1979; 101: 220-230.

[14] Greenwood JA, Williamson JBP. Contact of Nominally Flat Surface. Proc R Soc Lond A 1966; 295: 300-319.

[15] Kazama T, Yamaguchi A. Application of a Mixed Lubrication Model for Hydrostatic Thrust Bearing of Hydraulic Equipment. ASME J Tribol 1993; 115: 686-691.

[16] Guo Y, Lu X and Li W, et al. A mixed-lubrication model considering elastoplastic contact for a piston ring and application to a ring pack. Proc Inst Mech Eng Part D: J Automob Eng 2015; 229: 174-188.

[17] Nayak PR. Random Process Model of Rough Surfaces. AMSE J Lub Tech. 1971; 93: 398-407.

[18] Zhang X, Jackson RL. An Analysis of the Multiscale Structure of Surfaces with Various Finishes. Tribol Trans 2017; 60: 121-134.

[19] Zhang X, Xu Y and Jackson RL. An Analysis of Generated Fractal and Measured Rough Surfaces in Regards to Their Multi-scale Structure and Fractal Dimension. Tribol Int 2017;105: 94-101.

[20] Fardin N, Stephansson O and Jing L. The Scale Dependence of Rock Joint Surface Roughness. Int J Rock Mech Min 2001; 38: 659-669.

[21] McCool, JI. Relating Profile Instrument Measurements to the Functional Performance of Rough Surfaces. ASME J Tribol 1987;109: 264-270.

[22] Thomas, TR. Rough Surfaces, Longman, 1982.

[23] Zhang X, An Analysis of the Multi-scale Structure of Rough Surface. Master thesis, Auburn University, USA, 2014.

[24] Johnson, KL. Contact Mechanics, Cambridge University Press, 1985.

[25] Yastrebov VA, Anciaux G and Molinari J. From Infinitesimal to Full Contact Between Rough Surfaces: Evolution of the Contact Area. Int J Solids Struct 2015; 52: 83-102.

[26] Putignano C, Afferrante L and Carbone G, et al. A New Efficient Numerical Method for Contact Mechanics of Rough Surfaces. Int J Solids Struct 2012; 49: 338-343.

[27] Fournier A, Fussell D and Carpenter L. Computer Rendering of Stochastic Models. Graphics and Image Processing 1982; 25: 371-384.

[28] Saupe D. Algorithms for Random Fractals. In: Barnsley MF, Devaney RL, Mandelbrot BB, Peitgen H.-O, Saupe D, Voss RF. (eds) The Science of Fractal Images. New York: Springer, 1988, pp.71-136.

[29] Voss RF. Fractal in Nature: From Characterization to Simulation. In: Barnsley MF, Devaney RL, Mandelbrot BB, Peitgen H.-O, Saupe D, Voss RF. (eds) The Science of Fractal Images. New York: Springer, 1988, pp.21-70.

[30] Marak I., http://old.cescg.org/CESCG97/marak/node3.html (accessed 16 October 2018).